

HARD X-RAY EMISSION OF THE MICROQUASAR GRO J1655–40 DURING THE RISE OF ITS 2005 OUTBURST

A. JOINET,¹ E. KALEMCI,² AND F. SENZIANI^{3,4,5}

Received 2007 March 7; accepted 2008 January 21

ABSTRACT

We present an analysis of the high-energy emission of the Galactic black hole GRO J1655–40 at the beginning of its 2005 outburst. The data from 458 ks of *INTEGRAL* observations, spread over 4 weeks, are analyzed, along with the existing simultaneous *RXTE* and *Swift* data. The high-energy data allow us to detect the presence of a high-energy cutoff and to study its evolution during the outburst rise. This high-energy feature is generally related to thermal mechanisms in the framework of Comptonization models from which we can estimate the plasma parameters. We found an electron temperature of about 30–40 keV and an optical depth of around 1.8–2.1. The high-energy cutoff decreased along with the radio flux and disappeared as the jet turned off.

Subject headings: accretion, accretion disks — black hole physics — gamma rays: observations — stars: individual (GRO J1655–40) — X-rays: binaries

1. INTRODUCTION

GRO J1655–40 is a transient Galactic X-ray binary. Since its discovery on 1994 July 27 with BATSE (Zhang et al. 1994) on board the *Compton Gamma Ray Observatory* (CGRO), the source has undergone several outbursts (e.g., in 1995: see Zhang et al. 1997; in 1996/1997: see Kuulkers et al. 2000; Méndez et al. 1998). It is likely to be a low-mass X-ray binary, and the compact object in this system is probably a black hole (Bailyn et al. 1995) with a mass estimated at $6.3 M_{\odot}$ (Greene et al. 2001) and a distance of 3.2 kpc (Hjellming & Rupen 1995), on which we based our calculation of the Eddington luminosity, L_{Edd} , of this source. A recent work by Foellmi et al. (2006) places an upper limit of 1.7 kpc on the distance, but this upper limit is still under debate. Radio jets were discovered in the mid-1990s and revealed apparent superluminal motion in opposite directions (Tingay et al. 1995).

A transient Galactic black hole usually exhibits a complex spectrottemporal variability with the variation of the accretion rate. The changes in the black hole properties allow us to characterize the state of the source (see McClintock & Remillard [2006] for a complete description). In the high/soft state (HSS), the soft X-ray emission dominates the spectrum in the form of a blackbody component that is due to the thermal component from a standard accretion disk. In the low/hard state (LHS), the source is characterized by a relatively low flux in the soft X-rays ($\lesssim 1$ keV) and a high flux in the hard X-rays (~ 100 keV). This is usually interpreted (e.g., Shapiro et al. 1976; Narayan & Yi 1995) as the Comptonization of the soft X-ray photons emitted by a cold, geometrically thin disk (Shakura & Sunyaev 1973) by a hot plasma surrounding this accretion disk. The hard component is generally described by a power law with a photon index of $\Gamma = 1.4$ –1.8 and an exponential cutoff, E_c , at around 100–200 keV. In addition, a Fe K α line at ~ 6.4 keV and a Compton reflection bump peaking at ~ 30 keV may exist. These are signatures of the irradiation of

the cold, optically thick disk by the hard X-rays from the corona (George & Fabian 1991). The LHS is characterized by radio emission that has been shown to be consistent with a mildly relativistic ($v \simeq 0.6c$) jet (Gallo et al. 2003). Before entering into the HSS, the source may go through transitional states, also called intermediate states. Homan & Belloni (2005) divide the intermediate state into the hard intermediate state (HIMS) and the soft intermediate state (SIMS), which depend on the power density spectra and the spectral index. The jet starts to be quenched in the intermediate state (e.g., Corbel et al. 2004).

We present here an analysis of the spectral evolution of GRO J1655–40 during the rising phase of the 2005 outburst. The analysis is based on data taken by the *International Gamma-Ray Astrophysics Laboratory* (*INTEGRAL*; Winkler et al. 2003). GRO J1655–40 was observed by *INTEGRAL* from MJD 53425 (*INTEGRAL* revolution 289 on 2005 February 24) to MJD 53448 (*INTEGRAL* revolution 296 on 2005 March 19). The spectral and timing evolution of the source from the Proportional Counting Array (PCA) on board the *Rossi X-Ray Timing Explorer* (*RXTE*) in the 3–30 keV energy range has been studied in detail from MJD 53419 to MJD 53445 by Shaposhnikov et al. (2007). Brocksopp et al. (2006) presented the data from the Burst Alert Telescope (BAT) on board the *Swift* observatory in the 14–150 keV energy range from MJD 53430 to MJD 53435. Caballero García et al. (2007) presented the results of the analysis of 4 Target of Opportunity (ToO) observations from 2005 February 27 to 2005 April 11 using JEM-X, ISGRI, and SPI on board the *INTEGRAL* observatory and interpreted their data in the framework of several physical models. They came to the conclusion that no cutoff is necessary to describe the data in the LHS.

We studied the broadband spectral evolution using the spectrometer on board *INTEGRAL* (SPI; Vedrenne et al. 2003) in the 23–600 keV energy range, combined with all the publicly available data from the PCA and HEXTE detectors on board the *RXTE* observatory, as well as the BAT detector, in order to cover the 3–200 keV energy range. One of the main reasons for studying such a source during the transition from the LHS to the HSS is to follow the evolution of the high-energy cutoff. We propose to quantify its value, as well as its significance, during the rising phase of the outburst.

We briefly describe the data analysis methods for the *INTEGRAL* (SPI and IBIS/ISGRI), *RXTE* (PCA and HEXTE),

¹ Centre d’Etude Spatiale des Rayonnements (CESR), 9 Avenue du Colonel Roche, BP 4346, 31028 Toulouse, France.

² Sabancı University, Orhanlı-Tuzla, 34956 İstanbul, Turkey.

³ INAF-IASF Milano, via Bassini 15, 20133 Milano, Italy.

⁴ Université Paul Sabatier, 31062 Toulouse, France.

⁵ Università degli Studi di Pavia, Dipartimento di Fisica Nucleare e Teorica, via Bassi 6, 27100 Pavia, Italy.

TABLE 1
INTEGRAL OBSERVATIONS OF GRO J1655–40

| Revolution | SP _{start} | SP _{stop} | Δt_{sp} (ks) | ID | RX _{start} | RX _{stop} | Exp. (ks) |
|--|---------------------|--------------------|--------------------------------|----------------|---------------------|--------------------|--------------|
| 289..... | 53425.14 | 53427.36 | 133 | 90058-16-04-00 | 53425.06 | 53425.10 | 3.7 |
| | ... | ... | ... | 90428-01-01-00 | 53426.04 | 53426.28 | 20.6 |
| | ... | ... | ... | 90058-16-05-00 | 53427.02 | 53427.06 | 3.1 |
| 290..... | 53428.13 | 53430.36 | 134 | 90428-01-01-03 | 53428.14 | 53428.20 | 5.1 |
| | ... | ... | ... | 90428-01-01-04 | 53428.86 | 53429.12 | 22.5 |
| | ... | ... | ... | 90428-01-01-02 | 53429.71 | 53429.97 | 22.6 |
| 290 _{ibis} ^a | 53428.20 | 53429.50 | 69 | ... | ... | ... | ... |
| 291..... | 53432.85 | 53433.47 | 29 | 90428-01-01-10 | 53432.79 | 53433.00 | 17.97 |
| 292..... | 53434.80 | 53436.42 | 36 | 91404-01-01-02 | 53433.91 | 53434.09 | 16.14 |
| | ... | ... | ... | 91404-01-01-03 | 53434.69 | 53434.73 | 2.80 |
| | ... | ... | ... | 91404-01-01-01 | 53435.61 | 53435.64 | 2.37 |
| | ... | ... | ... | 91404-01-01-04 | 53436.16 | 53436.17 | 1.41 |
| 292 _{sw} -A,B..... | 53434.89 | 53436.45 | 17.75 | ... | ... | ... | ... |
| 293a..... | ... | ... | ... | 91702-01-01-00 | 53436.72 | 53436.81 | 7.4 |
| 293 _{sw} | 53436.48 | 53436.49 | 14.89 | ... | ... | ... | ... |
| 293..... | 53437.11 | 53438.34 | 51 | 91702-01-01-03 | 53438.05 | 53438.08 | 2.2 |
| 294a..... | ... | ... | ... | 91704-04-01-00 | 53439.61 | 53439.65 | 3.4 |
| 294b..... | ... | ... | ... | 91704-04-01-01 | 53439.74 | 53439.78 | 3.6 |
| 294 _{sw} -A..... | 53439.05 | 53439.65 | 13.29 | ... | ... | ... | ... |
| 294 _{sw} -B..... | 53440.72 | 53441.87 | 4.42 | ... | ... | ... | ... |
| 294-B..... | ... | ... | ... | 91702-01-02-01 | 53441.51 | 53441.54 | 2.3 |
| | ... | ... | ... | 91702-01-02-02 | 53441.59 | 53441.60 | 1.4 |
| | ... | ... | ... | 91702-01-02-03 | 53441.98 | 53442.01 | 2.2 |
| 294-C..... | ... | ... | ... | 91702-01-02-04 | 53442.06 | 53442.07 | 1.8 |
| | ... | ... | ... | 91702-01-02-05 | 53442.12 | 53442.14 | 1.5 |
| | ... | ... | ... | 91702-01-02-06 | 53442.58 | 53442.66 | 6.9 |
| 295-A..... | ... | ... | ... | 91702-01-03-00 | 53443.54 | 53443.80 | 22.5 |
| (295+296) _{sw} | 53444.92 | 53447.21 | 15.33 | ... | ... | ... | ... |
| 295+296..... | 53445.07 | 53447.71 | 75 | 91702-01-04-01 | 53444.49 | 53444.50 | 0.6 |
| (295+296) _{ibis} ^a | 53445.10 | 53447.80 | 72 | ... | ... | ... | ... |

NOTES.—For each *INTEGRAL* revolution, we give the beginning (SP_{start}) and the end (SP_{stop}) of the *INTEGRAL* observations, in units of MJD, from the SPI detector. Revolutions 295 and 296 have been merged (295+296). The quantity Δt_{sp} is the useful duration for the *INTEGRAL* observations. “ID” is the identification program number of the *RXTE* observations. RX_{start} and RX_{stop} indicate the beginning and the end of the *RXTE* observations taken quasi-simultaneously with the *INTEGRAL* observations. “Exp.” indicates the exposure time for the PCA. We indicate the simultaneous BAT data by adding the subscript “sw” to the number of the revolution. The details of the BAT observations are given in Table 2. We indicate with horizontal lines the observation periods for which the source was in the same X-ray state (see § 3.1 and Fig. 1).

^a As the observation period was not the same for the SPI and IBIS/ISGRI detectors, we indicate the IBIS data with a separate subscript: revolutions 290_{ibis} and (295+296)_{ibis}.

and *Swift* (BAT) data in § 2. The scientific results from the spectral modeling are presented in § 3.

2. OBSERVATIONS AND DATA REDUCTION

GRO J1655–40 started a new outburst on 2005 February 17 (MJD 53418), which was observed by Markwardt et al. (2005) with the PCA detector on board the *RXTE* observatory. This reactivation was confirmed by Torres et al. (2005), who reported the near-infrared activity of the source on 2005 February 21. *INTEGRAL* performed follow-up observations on GRO J1655–40 starting at MJD 53425. Table 1 gives the details of the observations from each *INTEGRAL* revolution and the corresponding quasi-simultaneous *RXTE* observations used in this analysis.

2.1. *INTEGRAL* Data Reduction

The data from the SPI detector were reduced as explained in Joinet et al. (2005), except that only 17 detectors were active, compared to 19 at the beginning of the mission. The SPIROS V6 algorithm has been used in order to derive the position of the sources detected in the field of view of GRO J1655–40. We refer to § 2.1.1 of Joinet et al. (2005) for the method of the spectral

reconstruction. Only pointings for which GRO J1655–40 was at a distance of less than 12° from the central axis were taken into account for the analysis. We excluded pointings that were affected by a solar flare or by exit/entry into the radiation belts. We obtained 458 ks of useful data during the observation period covered by revolutions 289–296 (see Table 1). Revolutions 295 and 296 have been merged and are referred to as 295+296. The variability timescale of each source was estimated (see § 3.1) on the basis of both its intensity and its known temporal behavior. The background flux is stable within each of the considered revolutions except for revolutions 292 and 293, for which a variability timescale of one pointing (with a duration of 30–40 minutes) was used. We consider only one normalization parameter per orbit, with an uniformity map determined for the 17 detector configuration.

We limited the energy range from 23 to 600 keV for the SPI data and added a 3% systematic error to all spectral channels. The IBIS/ISGRI data corresponding to revolutions 290, 295, and 296, which were published by Caballero García et al. (2007), have also been included in the analysis. We used their high-level results, and they used the Standard Off-Line Science Analysis (OSA) 5.1 software package.

TABLE 2
DETAILS OF BAT DATA OBSERVATIONS

| Revolution | ID | Sw _{start} | Sw _{stop} | Exp. (ks) |
|-------------------------------|-------------|---------------------|--------------------|--------------|
| 292 _{sw} -A | 00106709002 | 53434.89 | 53434.91 | 1.35 |
| | 00106709003 | 53435.23 | 53435.24 | 1.35 |
| | 00030009002 | 53435.42 | 53435.50 | 2.94 |
| | 00106709004 | 53435.76 | 53435.78 | 0.90 |
| | 00055750001 | 53436.08 | 53436.09 | 0.90 |
| | 00055750002 | 53436.15 | 53436.16 | 1.30 |
| | 00055750003 | 53436.21 | 53436.23 | 1.35 |
| 292 _{sw} -B | 00106709005 | 53436.23 | 53436.25 | 1.35 |
| | 00055750004 | 53436.28 | 53436.30 | 1.35 |
| | 00058739002 | 53436.30 | 53436.32 | 1.66 |
| | 00055750005 | 53436.35 | 53436.35 | 0.64 |
| | 00058739002 | 53436.37 | 53436.38 | 1.04 |
| | 00055750006 | 53436.41 | 53436.42 | 0.64 |
| | 00058739002 | 53436.44 | 53436.45 | 0.98 |
| 293 _{sw} | 00055750007 | 53436.48 | 53436.49 | 0.64 |
| | 00055750008 | 53436.54 | 53436.55 | 0.45 |
| | 00107547001 | 53436.62 | 53437.17 | 18.30 |
| 294 _{sw} -A | 00107547002 | 53439.05 | 53439.65 | 13.29 |
| 294 _{sw} -B | 00058736001 | 53440.72 | 53440.93 | 1.80 |
| | 00058746001 | 53440.98 | 53441.00 | 1.80 |
| | 00058746002 | 53441.07 | 53441.87 | 0.82 |
| (295+296) _{sw} | 00055800001 | 53444.92 | 53445.13 | 1.24 |
| | 00111063001 | 53446.14 | 53446.88 | 12.60 |
| | 00058752001 | 53447.06 | 53447.21 | 1.49 |

NOTES.—We give the observation ID number, the beginning (Sw_{start}) and the end (Sw_{stop}) of the BAT observations in units of MJD, and the net exposure time. Revolutions 295 and 296 have been merged, and their data set is named (295+296)_{sw}. We indicate with horizontal lines the observation periods for which the source was in the same X-ray state (see § 3.1 and Fig. 1).

2.2. RXTE Data Reduction

We also analyzed the public data from the PCA and HEXTE detectors on board the *RXTE* observatory (Bradt et al. 1993; Rothschild et al. 1998). For both instruments, the data reductions were performed using the FTOOLS routines in the HEASoft software package distributed by NASA's HEASARC (ver. 6.0.4). Table 1 summarizes the set of *RXTE* observations performed contemporaneously with the *INTEGRAL* data observation periods, except for revolution 294, for which there are no *INTEGRAL* data available. This observation period has been divided into two data sets. Several *RXTE* observations have been merged in order to correspond to one integrated *INTEGRAL* revolution.

All available PCUs of the PCA (Bradt et al. 1993) detector have been used for the data extraction. We added 0.8% as systematic error up to 7 keV and 0.4% as systematic error above 7 keV (Tomsick et al. 2001).

For HEXTE, we used the response matrix created by the FTOOLS and applied the necessary dead-time correction (Rothschild et al. 1998). The HEXTE background is measured throughout the observation by alternating between the source and background fields every 32 s. The data from the background regions are merged.

We limited the energy range from 3 to 25 keV and from 16 to 227 keV for the PCA and HEXTE data, respectively. The HEXTE channels were grouped by 2 for channels 16–31, by 4 for channels 32–59, by 10 for channels 60–99, and by 64 for channels 100–227.

2.3. Swift Data Reduction

All the publicly available data from the BAT detector on board the *Swift* observatory (Gehrels et al. 2004; Barthelmy et al. 2005) covering the rising phase of the 2005 outburst were also analyzed (see Table 2). Some of them were simultaneous with certain *INTEGRAL* revolutions (292 and 295+296). Revolution 292 has been divided into two data sets composed of seven BAT pointings, with a duration of 10.09 ks for 292_{sw}-A and 7.66 ks for 292_{sw}-B. We also used the *Swift* data covering the observation period between *INTEGRAL* revolutions 292 and 293 (293_{sw}) and between revolutions 293 and 295-B (294_{sw}-A and 294_{sw}-B). We reduced the data using the standard *Swift* software⁶ (ver. 2.4). A standard filtering was applied in order to discard the data affected by high background rates and source occultations. For each interval over which the BAT pointings were unchanged, we extract a background-subtracted spectrum together with the response matrix, using the mask-weighting technique. Systematic errors were applied to the spectra using the batphaseserr BAT FTOOL. For the spectral analysis, we limited the energy range from 16 to 150 keV. For both the *RXTE* instruments and the BAT, the normalization factor was set free with respect to the SPI normalization for all fits.

3. RESULTS

3.1. Light Curve

The flux extraction for GRO J1655–40 from the SPI observations was performed by taking into account the hard X-ray sources detected in the field of view of the source. We used a timescale of one pointing (whose duration is about 3600 s) for 4U 1700–377 and OAO 1657–415 and two pointings for GX 340+0 and 4U 1705–322. We also considered other sources (GRO J1655–40, 1E 1740–2942, 4U 1630–47, GX 337+00, and GX 349+2) with a constant flux within each revolution. As the significance of the sources decreases above 150 keV, we considered only two sources with a timescale resolution of 3600 s for 4U 1700–77, and one revolution for GRO J1655–40, to extract fluxes in the 150–600 keV energy range. The light curve of the source from revolution 289 up to revolution 296 in the 23–51 keV energy range is shown in Figure 1. As the source was in the border of the SPI field of view between *INTEGRAL* revolutions 293 and 295-B, we used the *RXTE* and BAT observations (294_{sw}-A and 294_{sw}-B) to cover this period. Table 3 gives the SPI and BAT fluxes in different energy bands.

We also extracted the light curve obtained by the *RXTE* all-sky monitor (ASM) in the 1.5–12 keV energy range during the same period (with data taken from the public *RXTE* database⁷). The different states harbored by the source were determined by Shaposhnikov et al. (2007) on the basis of the X-ray properties from the PCA observations and are also summarized in Figure 1. The source was in the LHS from revolution 289 up to revolution 292, after which it entered the HIMS during revolution 293 (also observed by the BAT detector: see data sets 293_{sw} and 294_{sw}-A), the SIMS during revolution 294-B, and was in the HSS from revolution 295-C onward. Revolution 294 has been divided into two *RXTE* data sets (294-B and 294-C) in order for us to follow the evolution of the high-energy cutoff during the SIMS.

As can be seen from the SPI light curve (Fig. 1), the 23–51 keV flux increased by a factor of 2.9 between MJD 53425 ($\phi = 42 \pm 2$ mcrab) and MJD 53433 ($\phi = 121 \pm 7$ mcrab), while the source

⁶ Available at <http://swift.gsfc.nasa.gov/docs/software/lheasoft>.

⁷ See <http://xte.mit.edu/lcextrect/asmsel.html>.

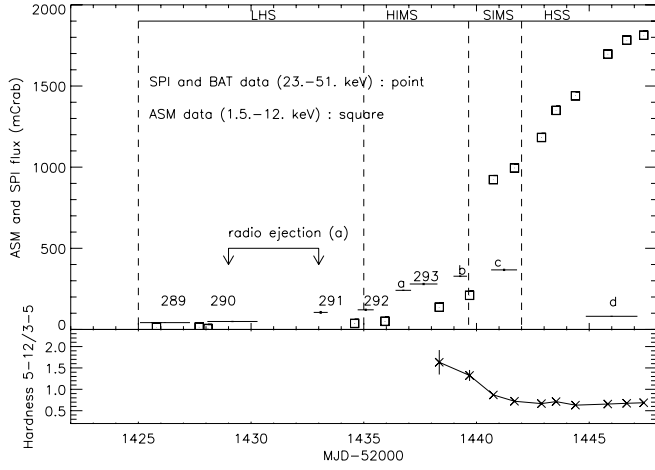


FIG. 1.—*Top*: ASM (1.5–12 keV) and SPI (23–51 keV) light curves of GRO J1655–40 during the rising phase of the 2005 outburst. The legend of letters is as follows: “a” is 293_{sw}, “b” is 294_{sw-A}, “c” is 294_{sw-B}, and “d” is (295+296)_{sw}. The flux of points a, b, c, and d has been extracted from BAT observations. The different states harbored by the source are summarized on the graph (see text for the definition): “LHS” is the low/hard state, “HIMS” is the hard intermediate state, “SIMS” is the soft intermediate state, and “HSS” is the high/soft state. Two arrows indicate the period associated with a radio flare event [labeled “(a)”]; see text]. *Bottom*: Evolution of the hardness from the ASM in the 3–12 keV energy range, which is defined as the ratio of the ASM fluxes ϕ in two energy ranges: $\phi(5\text{--}12\text{ keV})/\phi(3\text{--}5\text{ keV})$.

was in the LHS. A radio ejection was observed between MJD 53429 and 53433, with a radio peak at 5 GHz (Shaposhnikov et al. 2007). After this ejection, the X- and γ -ray flux increased exponentially until *INTEGRAL* revolution 293 or MJD 53437–53438 ($\phi = 280 \pm 7$ mcrab), during which time the source was in the HIMS. As the flux in the 3–25 keV energy range measured from PCA data increased by a factor of 3.9, the flux in the 23–51 keV energy range decreased by a factor of 3.5 between revolution 293 and revolution (295+296)_{sw}, indicating the transition from the LHS to the HSS.

3.2. Spectral Modeling of the X- and γ -Ray Data

The spectra corresponding to each set of data in Tables 1 and 2 have been fitted with various models available in the standard XSPEC 11.3.1 fitting package (Arnaud 1996). In all fits, the iron emission line was modeled by a narrow Gaussian line fixed at an energy of 6.4 keV with a free width. For all models, the inner disk inclination was fixed at 70° (van der Hooft et al. 1998). We also consider the emission from a multicolor disk blackbody (DISKBB

in XSPEC; Mitsuda et al. 1984). We account for the interstellar absorption (PHABS in XSPEC) using a hydrogen column density of $N_H = 7 \times 10^{21} \text{ cm}^{-2}$ for most of the observations (see § 3.2.1 for exceptions), which is based on the values constrained by *XMM-Newton* observations during the 2005 outburst (Diaz Trigo et al. 2007).

3.2.1. Power Law with a Cutoff

First, a power-law component is added to the base model described above. The best-fit parameters are presented in Table 4. During the LHS (revolutions 289, 290, 291, and 292), we found a constant spectral index of $\Gamma \simeq 1.47$ (with a reduced χ^2 value ranging from 1.7 up to 2.0).

During revolutions 289, 290, and 291, the fits are significantly improved, as can be seen from the reduced χ^2 values (with an *F*-test probability of less than 10^{-9}), by adding a high-energy cutoff component (see Table 4). A constant spectral index Γ of about 1.33–1.36 has been obtained, which is almost the same as the value found by Shaposhnikov et al. (2007; 1.35 ± 0.03). The high-energy cutoff value of $E_c = 231^{+94}_{-50}$ keV is consistent with the range value of 163–214 keV presented in Shaposhnikov et al. (2007) for revolution 289. The SPI data that we analyzed for all the outbursts allow us to constrain its value and to precisely describe its evolution, which was not done in Shaposhnikov et al. (2007). However, we reach a conclusion contrary to that of Caballero García et al. (2007), who showed that no cutoff was required to describe the data corresponding to revolution 290. We fit the data set corresponding to revolution 290 using the PCA, ISGRI, and SPI data with the model PHABS(DISKBB+POWERLAW)HIGHECUT in order to compare our results with the ones derived by Caballero García et al. (2007). We found a high-energy cutoff power law constrained to a value of 22^{+6}_{-8} keV and a folding energy of $E_{\text{fold}} = 193^{+14}_{-21}$ keV, with a reduced χ^2 of 0.83 (87 degrees of freedom [dof]). By fitting the ISGRI, HEXTE, and PCA data, we found a folding energy of $E_{\text{fold}} = 253^{+34}_{-31}$ keV and a photon index of $\Gamma = 1.40^{+0.02}_{-0.02}$ (with a reduced χ^2 of 1.43; 90 dof).

For revolution 292, the high-energy cutoff is constrained to a value of $E_c = 187^{+22}_{-20}$ keV. The BAT data were combined with the simultaneous PCA, HEXTE, and SPI data corresponding to *INTEGRAL* revolution 292 in order to check the cross-calibration between all instruments. During revolutions 289–292, the disk component was very weak. We then note a decrease of the high-energy cutoff value down to $E_c = 87^{+4}_{-5}$ keV during revolution 294a as the source transitions into the HIMS (Shaposhnikov et al.

TABLE 3
FLUX, ϕ (EXPRESSED IN UNITS OF mcrab), OF GRO J1655–40 MEASURED BY SPI
DURING DIFFERENT *INTEGRAL* REVOLUTIONS AND FOR SEVERAL ENERGY BANDS

| Revolution | ϕ (23–51 keV) | ϕ (51–95 keV) | ϕ (95–160 keV) | ϕ (160–270 keV) |
|--|-----------------------|-----------------------|------------------------|-------------------------|
| 289..... | 42^{+2}_{-2} | 64^{+6}_{-6} | 81^{+7}_{-7} | 59^{+16}_{-16} |
| 290..... | 49^{+4}_{-4} | 74^{+9}_{-9} | 89^{+7}_{-7} | 87^{+21}_{-21} |
| 291..... | 50^{+14}_{-14} | 116^{+30}_{-30} | 88^{+30}_{-30} | 167^{+70}_{-70} |
| 292..... | 125^{+8}_{-8} | 159^{+19}_{-19} | 245^{+25}_{-25} | 187^{+50}_{-50} |
| 293 _{sw} | 241^{+3}_{-4} | 320^{+7}_{-6} | 403^{+12}_{-12} | ... |
| 293..... | 280^{+7}_{-7} | 327^{+13}_{-13} | 358^{+14}_{-14} | 214^{+37}_{-37} |
| 294 _{sw-A} | 328^{+5}_{-5} | 357^{+7}_{-7} | 382^{+14}_{-12} | ... |
| 294 _{sw-B} | 367^{+6}_{-7} | 347^{+11}_{-10} | 332^{+17}_{-17} | ... |
| (295+296) _{sw} ^a | 81^{+3}_{-3} | 76^{+6}_{-6} | 73^{+10}_{-9} | ... |

NOTE.—We indicate with horizontal lines the observation periods for which the source was in the same X-ray state (see § 3.1 and Fig. 1).

^a These data correspond to those for revolutions 295 and 296, which have been merged.

TABLE 4

PCA, SPI, AND HEXTE DATA, FITTED SIMULTANEOUSLY USING THE XSPEC MULTICOMPONENT MODEL PHABS*(GAUSSIAN+DISKBB+POWERLAW)

| Revolution | T_{in} (keV) | N_{in} | Γ | E_c (keV) | W_{Fe} (eV) | χ^2 (dof) | F -Test | ϕ_p/ϕ_b |
|---|--|--|--|-------------------------------------|-------------------------------------|----------------|-----------|-----------------|
| 289..... | 1.29 ^{+0.12} _{-0.12} | 0.80 ^{+0.37} _{-0.23} | 1.47 ^{+0.02} _{-0.02} | ... | 76 ⁺⁶⁷ ₋₆₀ | 1.86 (79) | ... | ... |
| | 1.41 ^{+0.08} _{-0.14} | 1.41 ^{+0.49} _{-0.17} | 1.36 ^{+0.04} _{-0.04} | 231 ⁺⁹⁴ ₋₅₀ | 75 ⁺⁴² ₋₄₈ | 0.95 (78) | 3.62E–10 | 9.6 |
| 290..... | 1.20 ^{+0.08} _{-0.05} | 1.05 ^{+0.58} _{-0.31} | 1.47 ^{+0.01} _{-0.01} | ... | 75 ⁺³⁶ ₋₅₀ | 2.04 (79) | ... | ... |
| | 1.40 ^{+0.08} _{-0.09} | 1.21 ^{+0.33} _{-0.22} | 1.33 ^{+0.03} _{-0.03} | 259 ⁺⁶² ₋₄₁ | 76 ⁺⁴² ₋₄₀ | 0.86 (78) | 1.85E–16 | 9.6 |
| 290 ^a | 1.09 ^{+0.12} _{-0.11} | 1.15 ^{+0.73} _{-0.44} | 1.51 ^{+0.01} _{-0.01} | ... | 69 ⁺⁴¹ ₋₄₁ | 3.45 (108) | ... | ... |
| | 1.39 ^{+0.08} _{-0.07} | 1.32 ^{+0.34} _{-0.23} | 1.32 ^{+0.03} _{-0.03} | 200 ⁺²⁹ ₋₂₃ | 77 ⁺³⁸ ₋₇₇ | 1.37 (107) | 1.69E–23 | 9.7 |
| 291..... | 1.04 ^{+0.14} _{-0.15} | 2.64 ^{+3.27} _{-1.15} | 1.46 ^{+0.01} _{-0.01} | ... | 75 ⁺³⁶ ₋₅₀ | 1.60 (79) | ... | ... |
| | 1.40 ^{+0.12} _{-0.16} | 1.37 ^{+0.82} _{-0.32} | 1.34 ^{+0.03} _{-0.04} | 253 ⁺⁷⁶ ₋₄₈ | 78 ⁺⁴² ₋₄₂ | 0.85 (78) | 1.42E–12 | 8.7 |
| 292..... | 1.09 ^{+0.08} _{-0.08} | 4.32 ^{+1.87} _{-1.24} | 1.48 ^{+0.01} _{-0.01} | ... | 113 ⁺⁷² ₋₈₂ | 4.48 (77) | ... | ... |
| | 1.27 ^{+0.09} _{-0.08} | 4.49 ^{+1.42} _{-1.12} | 1.29 ^{+0.02} _{-0.02} | 187 ⁺²² ₋₂₀ | 177 ⁺⁸⁸ ₋₈₁ | 0.85 (76) | 2.27E–29 | 7.5 |
| 292 + 292 _{sw} | 1.27 ^{+0.09} _{-0.08} | 4.50 ^{+1.42} _{-1.12} | 1.29 ^{+0.02} _{-0.02} | 186 ⁺²² ₋₁₈ | 76 ⁺⁴² ₋₄₀ | 0.68 (223) | ... | ... |
| 293 _{sw} + 293a..... | 0.93 ^{+0.06} _{-0.06} | 22 ⁺⁹ ₋₅ | 1.53 ^{+0.01} _{-0.01} | ... | 145 ⁺⁷⁵ ₋₅₂ | 3.85 (118) | ... | ... |
| | 1.07 ^{+0.05} _{-0.05} | 22 ⁺⁵ ₋₄ | 1.33 ^{+0.02} _{-0.02} | 173 ⁺²¹ ₋₁₇ | 315 ⁺⁹³ ₋₅₇ | 1.35 (117) | 1.19E–28 | 7.4 |
| 293..... | 1.60 ^{+0.05} _{-0.01} | 4.87 ^{+1.52} _{-0.76} | 1.62 ^{+0.05} _{-0.05} | ... | 388 ⁺⁴⁶ ₋₃₉ | 5.30 (77) | ... | ... |
| | 1.00 ^{+0.03} _{-0.03} | 45 ⁺²¹ ₋₁₅ | 1.37 ^{+0.02} _{-0.03} | 131 ⁺¹³ ₋₁₁ | 386 ⁺⁸⁰ ₋₅₂ | 1.15 (76) | 3.46E–27 | 5.3 |
| 294 _{sw} -A + 294a,b..... | 0.67 ^{+0.03} _{-0.03} | 286 ⁺¹⁷ ₋₁₄ | 1.82 ^{+0.3} _{-0.02} | ... | 166 ⁺²⁸ ₋₃₈ | 14.32 (118) | ... | ... |
| 294-B + 294 _{sw} -B..... | 1.01 ^{+0.03} _{-0.03} | 121 ⁺¹⁷ ₋₁₄ | 1.41 ^{+0.3} _{-0.02} | 87 ⁺⁴ ₋₅ | 646 ⁺⁶⁷ ₋₄₆ | 1.37 (117) | ... | 4.4 |
| | 0.98 ^{+0.01} _{-0.01} | 1681 ⁺⁶⁴ ₋₆₆ | 2.18 ^{+0.01} _{-0.02} | ... | 622 ⁺³⁵ ₋₄₄ | 1.16 (118) | ... | ... |
| | 0.98 ^{+0.01} _{-0.01} | 1687 ⁺⁶⁵ ₋₆₁ | 2.08 ^{+0.05} _{-0.04} | 302 ⁺²²⁵ ₋₈₁ | 673 ⁺⁵⁰ ₋₄₁ | 0.99 (117) | 1.682E–05 | 0.41 |
| 294-C..... | 1.02 ^{+0.01} _{-0.01} | 1686 ⁺⁵⁴ ₋₆₇ | 2.15 ^{+0.01} _{-0.01} | ... | 522 ⁺¹⁷⁴ ₋₁₀₈ | 1.96 (62) | ... | ... |
| | 1.02 ^{+0.01} _{-0.01} | 1676 ⁺⁶¹ ₋₅₇ | 2.08 ^{+0.02} _{-0.04} | 439 ⁺⁴¹⁸ ₋₁₅₃ | 538 ⁺³⁵ ₋₄₉ | 1.81 (61) | 1.49E–02 | 0.29 |
| 295-A..... | 1.09 ^{+0.01} _{-0.01} | 1709 ⁺⁶⁰ ₋₄₇ | 2.02 ^{+0.01} _{-0.01} | >800 | 340 ⁺³⁸ ₋₃₇ | 1.40 (62) | ... | 0.15 |
| 295-B + 295 _{sw} | 1.15 ^{+0.01} _{-0.01} | 1454 ⁺⁶³ ₋₂₉ | 1.85 ^{+0.07} _{-0.05} | >261 | 103 ⁺⁵⁰ ₋₅₀ | 1.03 (135) | ... | 0.05 |
| | 1.15 ^{+0.01} _{-0.01} | 1464 ⁺³⁷ ₋₂₇ | 1.87 ^{+0.04} _{-0.05} | ... | 110 ⁺⁹¹ ₋₈₀ | 1.02 (136) | ... | 0.05 |
| (295+296) _{all} ^a | 1.13 ^{+0.01} _{-0.01} | 1760 ⁺²⁰ ₋₉ | 2.17 ^{+0.01} _{-0.01} | ... | 188 ⁺⁵² ₋₄₅ | 0.86 (167) | ... | 0.07 |
| | 1.14 ^{+0.01} _{-0.01} | 1649 ⁺²³¹ ₋₁₃₄ | 2.05 ^{+0.11} _{-0.07} | >237 | 167 ⁺⁴⁶ ₋₄₄ | 0.84 (166) | ... | 0.05 |

NOTES.— T_{in} is the inner disk temperature, and N_{in} is the normalization. A Gaussian line was fixed at an energy of 6.4 keV, with a width fixed to 0.1 keV for revolutions 289 and 290. W_{Fe} is the equivalent width. The interstellar absorption PHABS is fixed to $0.7 \times 10^{22} \text{ cm}^{-2}$ until the data set 294_{sw}-A + 294a,b and to $0.5 \times 10^{22} \text{ cm}^{-2}$ from revolution 294-B onward. Γ is the photon index. The POWERLAW component was replaced by a CUTOFFPL component, and E_c is the high-energy cutoff. The F -test is calculated between the POWERLAW and CUTOFFPL models. We also give the ratio ϕ_p/ϕ_b , where ϕ_p and ϕ_b are the power-law and the blackbody fluxes in the 2–20 keV energy range, respectively. The quantity χ^2 (dof) is the reduced χ^2 with the associated degrees of freedom. For revolutions 295 and 296, which have been merged, both the SPI (295+296) and the *Swift* [(295+296)_{sw}] data have been used. This data set is named (295+296)_{all}. We indicate with horizontal lines the observation periods for which the source was in the same X-ray state (see § 3.1 and Fig. 1).

^a For revolution 290, as well as for the data set (295+296)_{all}, the IBIS/ISGRI data have been included [290_{ibis} and (295+296)_{ibis}].

2007). The disk component also became stronger, whereas the power-law index remained constant.

By fitting simultaneously the BAT, PCA, and HEXTE data for revolution 294 (data sets 294-B and 294_{sw}-B), when the source has entered the SIMS, a pure power law results in a reduced χ^2 value of 1.16 (118 dof). Adding a high-energy cutoff results in a significant reduction in the reduced χ^2 value (0.99; 117 dof), but the folding energy is not well constrained ($E_{\text{fold}} = 302^{+225}_{-81} \text{ keV}$) and strongly depends on the power-law index. The disk component also starts to dominate the energy spectrum, as can be seen from the clear changes in the ϕ_p/ϕ_b ratio (Table 4), where ϕ_p is the power-law flux and ϕ_b is the blackbody flux in the 2–20 keV energy range. This ratio decreases by a factor of 13 between revolutions 293 and 294-B due to an increase of the disk component ϕ_b by a factor of 21. The contribution of the hard component with respect to the disk component is lower than 50% during revolution 294-B. Moreover, the photon index becomes steeper, with $\Gamma \simeq 2.1$, indicating a spectral transition.

From data set 294-C, for which only PCA and HEXTE data are available, there is no evidence of a high-energy cutoff up to 286 keV. The reduced χ^2 value decreases from 2.00 (61 dof) down to 1.81 (61 dof) and from 1.66 (62 dof) down to 1.40 (62 dof) for data sets 294-C and 295-A, respectively, using $N_{\text{H}} = 5 \times 10^{21} \text{ cm}^{-2}$. The high value of the reduced χ^2 is due to

poor modeling of the low-energy part of the spectra. A complex spectral feature around 7 keV has been fitted by Díaz Trigo et al. (2007), using *XMM-Newton* and *INTEGRAL* data. The spectra corresponding to these fit parameters (Table 4) are shown in Figures 2 and 3.

3.2.2. Reflection Model PEXRAV

We fitted all data with a reflection model, PEXRAV in XSPEC (Magdziar & Zdziarski 1995), consisting of a power law with a high-energy cutoff and reflection from the neutral medium (see Table 5). During the LHS, as the luminosity in the 3–600 keV energy range increased by a factor of $\simeq 2.8$ from revolution 289 up to revolution 292, the spectral index is constant ($\Gamma \simeq 1.3$ –1.4). Similar values of the spectral index and of the high-energy cutoff are found by using the CUTOFFPL and the PEXRAV models; this can be explained by the fact that the reflection fraction is so low that an additional reflection component is not required in the fit. The range of values for the high-energy cutoff (180–380 keV) is consistent with the results of Shaposhnikov et al. (2007; $196 \pm 48 \text{ keV}$) for revolution 289. We determine an upper limit on the energy cutoff when the source is into the HSS of $E_c > 2000 \text{ keV}$ for the data set (295+296)_{all} (see Table 5).

During all observations (from the LHS to the HSS), the reflection component is not constrained and does not exceed

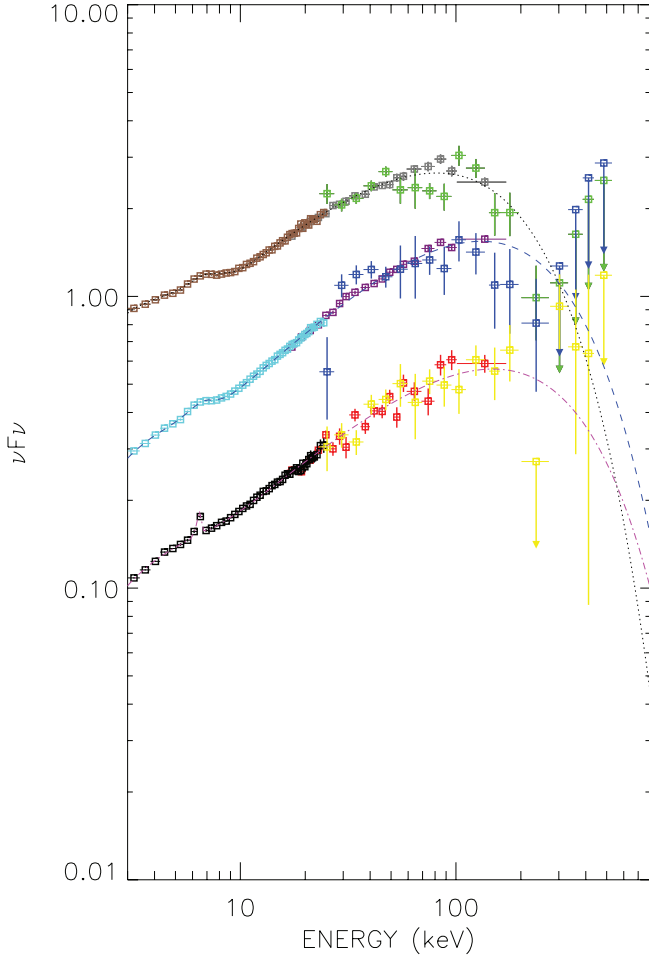


FIG. 2.—Spectra of GRO J1655–40 from PCA, SPI, and HEXTE data fitted simultaneously with the model described in Table 4. We show PCA data for revolutions 289 (black), 292 (cyan), and 293 (brown); HEXTE data for revolutions 289 (red), 292 (purple), and 293 (gray); and SPI data for revolutions 289 (yellow), 292 (blue), and 293 (green).

$\Omega = 0.2$, which is lower than the value of $\Omega \simeq 0.5$ found by Shaposhnikov et al. (2007).

3.2.3. Comptonization Model COMPTT

The hard power-law plus cutoff model of the LHS is usually interpreted as thermal Comptonization in a hot ($kT_e \sim 100$ keV), optically thin plasma (the corona). We used the COMPTT model (Titarchuk 1994) in order to describe the high-energy spectrum. The inner temperature of the disk (T_{in}) of the multicolor disk blackbody model is forced to be equal to the soft photon temperature (T_0) of the Comptonization model. We see in Table 6 that the optical depth is $\tau \simeq 1.8\text{--}2.0$, while the temperature decreases from $kT_e \simeq 40$ keV down to $kT_e \simeq 30$ keV from the LHS to the HIMS. By freezing the temperature to $kT_e = 37$ keV, which is the value obtained by Shaposhnikov et al. (2007) for the data set corresponding to *INTEGRAL* revolution 289, we determined an optical depth of $\tau = 1.98^{+0.05}_{-0.05}$, which is lower by a factor of 2.2 compared to the value found by Shaposhnikov et al. Moreover, the inner disk temperature T_{in} is higher: $T_{\text{in}} = 0.83$ keV instead of $T_{\text{in}} = 0.60$ keV. This could be explained by the fact that the continuum above 100 keV that is constrained by the *INTEGRAL* data is different in this reference.

Regardless of the fit models, we can describe the spectral evolution in terms of an evolution of the geometry based on the Compton parameter $y = (4kT/m_e c^2) \max(\tau, \tau^2)$ (where the

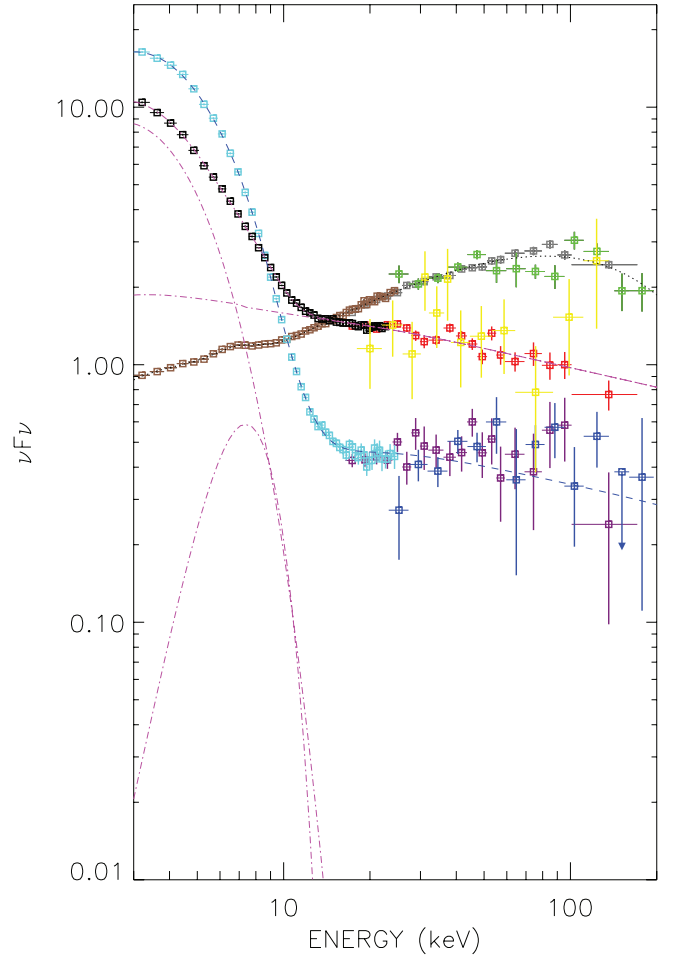


FIG. 3.—Same as Fig. 2, but for PCA data for revolutions 293 (brown), 294-B (black), and 295+296 (cyan); HEXTE data for revolutions 293 (gray), 294-B (red), and 295+296 (purple); SPI data for revolutions 293 (green) and 295+296 (blue); and BAT data for revolution 294_{SW-B} (yellow).

electronic temperature kT and the optical depth τ are derived from a Comptonization model; Sunyaev & Titarchuk 1980). During the LHS, the Compton parameter does not vary significantly ($y \simeq 0.6$). It starts to decrease during the HIMS (revolution 293), and this is correlated with the increase of the normalization of the disk component. It decreases (see Table 6) by a factor of 4.3 between revolution 289 and revolution 294-B, when the source transitions into the SIMS. The transition from the LHS to the intermediate states (both HIMS and SIMS) corresponds to a gradual decrease of the inner radius of the cold accretion disk, which is associated with either the cold disk penetrating the hot inner flow, or the latter collapsing into an optically thick accretion disk with small active regions of hot plasma on top of it (Zdziarski et al. 2002). The enhanced soft photon flux from the disk tends to cool down the hot phase, leading to softer spectra. This can be directly observed from the evolution of the blackbody component with respect to the power-law component (see the ratio ϕ_p/ϕ_b in Table 4).

4. DISCUSSION

4.1. High-Energy Cutoff and Jet Quenching

We determined that all data sets for the low/hard state require a high-energy cutoff. In addition to F -tests that indicate that the cutoffs are required, we have produced contour plots of the cutoff

TABLE 5

PCA, HEXTE, AND SPI DATA, FITTED SIMULTANEOUSLY USING THE XSPEC MULTICOMPONENT MODEL PHABS*(PEXRAV+GAUSSIAN+DISKBB)

| Revolution | Γ | E_c (keV) | T_{in} (keV) | N_{in} | W_{Fe} (eV) | χ^2 (dof) | $L_{3-600} \times 10^{-9}$ (ergs cm ⁻² s ⁻¹) |
|---|--|------------------------------------|--|--|------------------------------------|----------------|--|
| 289..... | 1.36 ^{+0.04} _{-0.08} | 237 ⁺¹⁴³ ₋₅₅ | 1.38 ^{+0.12} _{-0.11} | 1.07 ^{+0.48} _{-0.27} | 80 ⁺⁶⁵ ₋₇₈ | 0.98 (77) | 2.9 ^{+0.1} _{-0.1} |
| 290..... | 1.33 ^{+0.01} _{-0.06} | 255 ⁺¹⁰⁸ ₋₃₅ | 1.44 ^{+0.05} _{-0.11} | 1.07 ^{+0.26} _{-0.15} | 71 ⁺⁵⁵ ₋₆₁ | 0.89 (77) | 3.5 ^{+0.1} _{-0.1} |
| 290 ^a | 1.33 ^{+0.08} _{-0.01} | 207 ⁺¹¹¹ ₋₁₆ | 1.32 ^{+0.04} _{-0.01} | 1.68 ^{+0.56} _{-0.51} | 86 ⁺⁶² ₋₇₈ | 1.40 (106) | 3.3 ^{+0.02} _{-0.2} |
| 291..... | 1.37 ^{+0.10} _{-0.02} | 316 ⁺²³² ₋₂₃ | 1.36 ^{+0.17} _{-0.26} | 2.36 ^{+3.81} _{-0.90} | <130 | 0.85 (77) | 6.4 ^{+0.5} _{-0.6} |
| 292..... | 1.29 ^{+0.03} _{-0.02} | 185 ⁺³⁰ ₋₁₉ | 1.27 ^{+0.10} _{-0.08} | 5.73 ^{+1.80} _{-1.43} | <173 | 0.93 (77) | 8.1 ^{+0.4} _{-0.1} |
| 293 _{sw} + 293a..... | 1.33 ^{+0.07} _{-0.02} | 171 ⁺⁵⁹ ₋₁₅ | 1.07 ^{+0.05} _{-0.05} | 22 ⁺⁵ ₋₄ | 317 ⁺⁸⁰ ₋₅₀ | 1.36 (116) | 10.6 ^{+0.6} _{-0.3} |
| 293..... | 1.37 ^{+0.05} _{-0.05} | 131 ⁺¹⁴ ₋₈ | 1.04 ^{+0.06} _{-0.04} | 48 ⁺¹⁸ ₋₁₆ | 381 ⁺⁸⁸ ₋₈₂ | 1.22 (77) | 13.9 ^{+0.5} _{-0.1} |
| 294 _{sw} -A + 294a,b..... | 1.42 ^{+0.05} _{-0.05} | 88 ⁺¹⁴ ₋₈ | 1.00 ^{+0.06} _{-0.04} | 121 ⁺¹⁸ ₋₁₆ | 645 ⁺⁵⁹ ₋₅₆ | 1.39 (16) | 15.35 ^{+0.1} _{-0.1} |
| 294-B + 294 _{sw} -B..... | 2.07 ^{+0.12} _{-0.01} | 289 ⁺¹⁵¹ ₋₃₆ | 0.97 ^{+0.01} _{-0.01} | 1752 ⁺²⁴ ₋₈₆ | 701 ⁺¹⁰⁰ ₋₇₅ | 1.06 (116) | 18.13 ^{+0.03} _{-0.03} |
| 295-A..... | 2.03 ^{+0.05} _{-0.01} | >700 | 1.09 ^{+0.01} _{-0.01} | 1709 ⁺⁵⁵ ₋₅₆ | >156 | 1.45 (60) | 23.39 ^{+0.25} _{-0.16} |
| 295-B + 295 _{sw} -B..... | 1.86 ^{+0.04} _{-0.12} | >457 | 1.15 ^{+0.01} _{-0.01} | 1457 ⁺⁶⁴ ₋₆₁ | 110 ⁺⁶⁰ ₋₆₁ | 1.03 (134) | 22.19 ^{+0.32} _{-0.11} |
| (295+296) _{all} ^a | 2.16 ^{+0.04} _{-0.11} | >2000 | 1.14 ^{+0.01} _{-0.01} | 1509 ⁺⁶⁷ ₋₅₈ | <840 | 0.82 (164) | 20.84 ^{+3.24} _{-1.72} |

NOTES.— Γ is the photon index, and E_c is the energy cutoff. T_{in} is the inner disk temperature and N_{in} is the normalization. The interstellar absorption PHABS has been fixed to 0.7×10^{22} cm⁻² until the data set 294_{sw}-A + 294a,b and to 0.5×10^{22} cm⁻² from revolution 294-B onward. The Gaussian line was fixed at an energy of 6.4 keV. W_{Fe} is the equivalent width. The reflection fraction $\Omega/2\pi$ has been found to have an upper value in the range 0.1–0.2. L_{3-600} is the luminosity of the source in the 3–600 keV energy range. χ^2 (dof) is the reduced χ^2 with the associated degrees of freedom. For revolutions 295 and 296, which have been merged, the SPI (295+296) and *Swift* data [(295+296)_{sw}] have been used. This data set is named (295+296)_{all}. We indicate with horizontal lines the observation periods for which the source was in the same X-ray state (see § 3.1 and Fig. 1).

^a For revolution 290, as well as for revolutions (295+296)_{all}, the IBIS/ISGRI data have been included [290_{ibis} and (295+296)_{ibis}].

versus the power-law index for each data set, and these also substantiated the existence of the cutoff in individual revolutions. In Figure 4, the contour plot corresponding to revolution 290 clearly shows that the high-energy cutoff is required during this observation period, which has also been studied by Caballero García et al. (2007), who claimed that no cutoff is required for this data set. The main difference between our analysis and theirs is that we used the PCA to constrain the low-energy part

of the spectrum, whereas Caballero García et al. (2007) used JEM-X.

For the PEXRAV and CUTOFF models, the data from data sets 294-B and 294-C indicate that either the high-energy cutoff increases significantly or the cutoff vanishes completely. Such evolution was observed for GX 339–4 in the HIMS (Belloni et al. 2005) and has now appeared in the SIMS in the case of GRO J1655–40.

TABLE 6

PCA, HEXTE, AND SPI DATA, FITTED SIMULTANEOUSLY USING THE XSPEC MULTICOMPONENT MODEL PHABS*(COMPTT+GAUSSIAN+DISKBB)

| Revolution | kT (keV) | τ | T_{in} (keV) | N_{in} | χ^2 (dof) | y |
|---|-------------------------------------|--|--|--------------------------------------|----------------|--|
| 289..... | 43 ⁺¹⁶ ₋₈ | 1.78 ^{+0.26} _{-0.37} | 0.83 ^{+0.04} _{-0.04} | 12 ⁺³ ₋₂ | 1.04 (79) | 1.07 ^{+0.40} _{-0.23} |
| 290..... | 40 ⁺⁶ ₋₄ | 1.92 ^{+0.13} _{-0.14} | 0.80 ^{+0.03} _{-0.03} | 16 ⁺³ ₋₂ | 0.93 (78) | 1.15 ^{+0.17} _{-0.12} |
| 290 ^a | 36 ⁺⁴ ₋₃ | 1.98 ^{+0.14} _{-0.12} | 0.76 ^{+0.01} _{-0.03} | 18 ⁺³ ₋₃ | 1.82 (106) | 1.12 ^{+0.13} _{-0.10} |
| 291..... | 36 ⁺¹² ₋₆ | 2.07 ^{+0.15} _{-0.17} | 0.78 ^{+0.07} _{-0.06} | 34 ⁺¹⁰ ₋₂₁ | 0.84 (77) | 1.21 ^{+0.40} _{-0.21} |
| 292..... | 35 ⁺² ₋₂ | 2.09 ^{+0.10} _{-0.07} | 0.80 ^{+0.02} _{-0.04} | 44 ⁺¹⁰ ₋₄ | 1.36 (77) | 1.20 ^{+0.07} _{-0.07} |
| 293 _{sw} + 293a..... | 31 ⁺² ₋₁ | 2.15 ^{+0.1} _{-0.1} | 0.77 ^{+0.02} _{-0.02} | 106 ⁺¹⁶ ₋₁₃ | 1.63 (117) | 1.12 ^{+0.07} _{-0.08} |
| 293..... | 31 ⁺² ₋₂ | 2.01 ^{+0.09} _{-0.09} | 0.74 ^{+0.10} _{-0.12} | 244 ⁺³³⁸ ₋₉₃ | 1.31 (77) | 0.98 ^{+0.06} _{-0.06} |
| 294 _{sw} -A + 294a,b..... | 26 ⁺² ₋₂ | 1.93 ^{+0.09} _{-0.09} | 0.76 ^{+0.10} _{-0.12} | 457 ⁺³³⁸ ₋₉₃ | 2.06 (117) | 0.76 ^{+0.06} _{-0.06} |
| 294-B + 294 _{sw} -B..... | 282 ⁺³⁸ ₋₄₁ | 0.03 ^{+0.01} _{-0.01} | 0.95 ^{+0.01} _{-0.01} | 2065 ⁺⁵¹ ₋₁₁₅ | 1.07 (117) | 0.06 ^{+0.01} _{-0.01} |
| 294-B + 294 _{sw} -B ^b | 59 ⁺³³ ₋₂₃ | 0.55 ^{+0.38} _{-0.21} | 0.95 ^{+0.03} _{-0.02} | 1183 ⁺²⁰⁰ ₋₂₂₁ | 0.75 (115) | 0.25 ^{+0.14} _{-0.14} |
| 294-C..... | 320 ⁺³⁴ ₋₉₂ | 0.02 ^{+0.02} _{-0.01} | 1.00 ^{+0.01} _{-0.01} | 1967 ⁺⁷²¹ ₋₅₈ | 1.91 (61) | 0.05 ^{+0.01} _{-0.03} |
| 294-C ^b | 86 ⁺⁶¹ ₋₃₈ | 0.43 ^{+0.51} _{-0.23} | 1.06 ^{+0.03} _{-0.03} | 1192 ⁺¹⁹⁷ ₋₁₇₂ | 1.26 (59) | <0.20 |
| 295-B + 295 _{sw} -B..... | 763 ⁺¹⁶¹ ₋₆₁₀ | <0.07 | 1.24 ^{+0.01} _{-0.01} | 1267 ⁺⁵² ₋₃₇ | 1.02 (135) | <0.06 |
| (295+296) _{all} ^a | 445 ⁺³⁴⁸ ₋₈₈ | <0.12 | 1.17 ^{+0.01} _{-0.01} | 1402 ⁺⁶³ ₋₄₈ | 1.04 (165) | <0.07 |

NOTES.—The interstellar absorption PHABS has been fixed to 0.7×10^{22} cm⁻² until the data set 294_{sw}-A + 294a,b and to 0.5×10^{22} cm⁻² from revolution 294-B onward. T_{in} is the inner disk temperature, N_{in} is the normalization, τ is the optical depth, and kT is the plasma temperature. The Compton parameter y (see the definition in the text) has also been determined. χ^2 (dof) is the reduced χ^2 with the associated degrees of freedom. For revolutions 295 and 296, which have been merged, both the SPI (295+296) and the *Swift* data [(295+296)_{sw}] have been used. This data set is named (295+296)_{all}. We indicate with horizontal lines the observation periods for which the source was in the same X-ray state (see § 3.1 and Fig. 1).

^a For revolution 290, as well as for the data set (295+296)_{all}, the IBIS/ISGRI data have been added [290_{ibis} and (295+296)_{ibis}].

^b For the data sets 294-B and 294-C, power-law components Γ of 3.86^{+0.12}_{-0.18} and 3.95^{+0.40}_{-0.35} have been added, respectively.

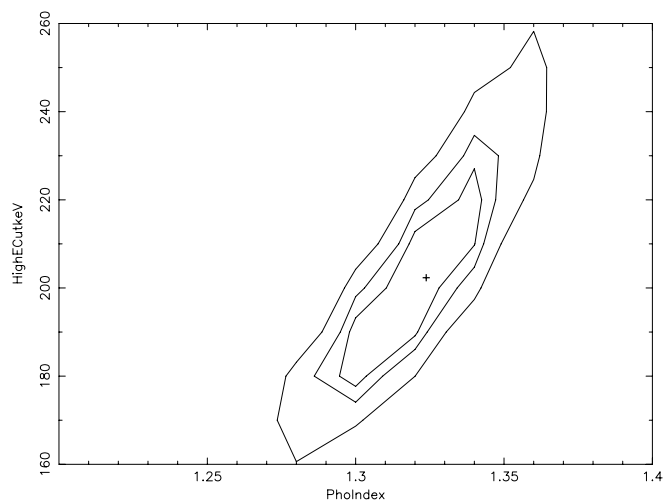


FIG. 4.—Contour plot of Γ - E_c (revolution 290) for the simultaneous PCA, HEXTE, ISGRI, and SPI observations, using the model described in Table 4. The curves refer to values of $\delta\chi^2 = 2.30, 4.61$, and 9.21 , which correspond to confidence levels of 68%, 90%, and 99%, respectively, for two interesting parameters.

We attempt to describe this high-energy feature by adding a power-law component to the Comptonization model COMPTT. We found that the addition of a power-law component leads to an improvement of the fit that is significant at the 99.9998% level for both data sets according to an F -test, with best-fit photon indexes of $\Gamma = 3.86^{+0.12}_{-0.18}$ and $\Gamma = 3.95^{+0.40}_{-0.35}$ for data sets 294-B and 294-C, respectively. The power-law component contributes at 23% and 20% of the 2–20 keV flux for revolutions 294-B and 294-C, respectively. The extension of a power law at high energy has already been observed in the steep power-law state of GRO J1655–40 during its 1996 outburst (see Remillard & McClintock 2006). It is interpreted as inverse Compton scattering that occurs in a nonthermal corona, which may be a simple slab operating on seed photons from the underlying disk (Zdziarski et al. 2005). The origin of the Comptonizing electrons is still a subject of debate. Poutanen & Fabian (1999) suggested that flare regions erupting from magnetic instabilities in the accretion disk could explain such a Comptonizing medium. The association of a nonthermal process with a state transition has also been discussed for Cyg X-1 (Malzac et al. 2006), in this case interpreting the power-law tail as the Comptonization of soft photons by accelerated electrons (see also Titarchuk 1997). Finally, such high-energy emission could also come from an optically thick electron-positron outflow covering the whole inner region of the accretion disk (Beloborodov 1999b).

As can be seen from Figure 5, there is a correlation between the radio intensity and the exponential energy cutoff. The maximum flux in the radio is achieved when the source is in the LHS. When the source enters the HIMS, the high-energy cutoff decreases (or the plasma cools down), as does the radio flux. Quenching of the jet in the soft states of black hole binaries is known to occur in many sources (Fender et al. 1999; Corbel et al. 2000). Here we show a clear evolutionary path to this quenching in terms of the plasma temperature, perhaps associated with the cooling and shrinking of the corona.

4.2. The Jet Ejection Event

The jet ejections usually occur at or near state transitions prior to the source entering the intermediate state (IS; Corbel et al. 2004). A radio flare ejection is observed for GRO J1655–40 during revolution 291, just before the X- and γ -ray flux peak.

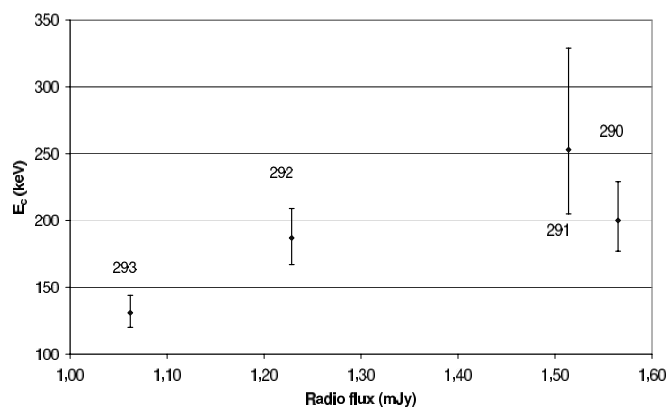


FIG. 5.—Evolution of the high-energy cutoff (E_c , expressed in units of keV) derived from the model given in Table 4 as a function of the radio flux measured by the VLA at 8.460 GHz (Shaposhnikov et al. 2007). The *INTEGRAL* revolution numbers are mentioned on the graph. There are no radio data available after revolution 293.

Such a behavior has also been observed for the black hole candidates H1743–322 and GX 339–4 (Joinet et al. 2005; Corbel et al. 2000; Fender et al. 1999) and could be linked to a coronal ejection event. The decrease of the Compton y -parameter (see Table 6) and the appearance of the nonthermal component (addition of the power-law component) indicate large changes in the corona geometry.

Moreover, the small reflection fraction combined with a high coronal temperature (or high-energy cutoff) can be explained by the model of Beloborodov (1999a), which argues that the corona above the accretion disk is fed by magnetic flares or by a nonstatic corona (Malzac et al. 2001). GRO J1655–40 started to enter the IS from the end of revolution 292. This state corresponds to the decay of the radio emission (Fig. 5), which is usually dominated by the decaying optically thin synchrotron emission from the jet ejections. During this state, such an emission is decoupled from the black hole system, as the emitting electrons are far from it. The radio emission is completely quenched starting from the SIMS (revolution 294-B).

5. CONCLUSION

We clearly observed a transition from the LHS to the HSS during the rising phase of the 2005 outburst of GRO J1655–40 between MJD 53425 and MJD 53445. The outburst was covered with SPI, HEXTE, PCA, and BAT, which allowed us to determine the high-energy cutoff with a high precision. During revolution 294, only data from the *RXTE* and *Swift* observatories were available to constrain the high-energy cutoff during an intermediate state. An evolution of the high-energy feature was noted during the LHS: it decreased from a value of about 200 keV down to 130 keV when the source reached its maximum luminosity in the γ -ray domain (above 23–600 keV). For the HSS, a lower limit for the high-energy cutoff has been determined. We deduced that there is no cutoff detectable in this spectral state. This decrease corresponds to a decrease in the radio flux, and the cutoff disappeared along with the radio jet. Finally, we also discussed the relation between state transitions and the emission of jets in X-ray binaries, which is a subject of great importance in order for us to have a complete view of the X-ray geometry. It would be interesting to perform a broadband spectral fitting (from radio up to the MeV range) in order to discriminate the different nonthermal processes suggested in this study.

The SPI project has been completed under the responsibility and leadership of the CNES. We are grateful to ASI, CEA, DLR, ESA, INTA, NASA, and OSTC for support.

Specific softwares used for this work have been developed by L. Bouchet. A. J. thanks N. Shaposhnikov and M. Rupen for all information concerning the radio detection, as well as M. D.

Caballero García, who provided the ISGRI data used in this paper. E. K. acknowledges the support of TÜBİTAK Career program 106T570, the Turkish National Academy of Sciences Young and Successful Scientist Award, and Marie Curie International Reintegration grant MIRG-CT-2005-017203. Finally, the authors are grateful to the anonymous referee for the very fruitful comments.

REFERENCES

- Arnaud, K. A. 1996, in ASP Conf. Ser. 101, *Astronomical Data Analysis Software and Systems V*, ed. G. H. Jacoby & J. Barnes (San Francisco: ASP), 17
- Bailyn, C., et al. 1995, *Nature*, 374, 701
- Barthelmy, S., et al. 2005, *Space Sci. Rev.*, 120, 143
- Belloni, T., Homan, J., Casella, P., van der Klis, M., Nespoli, E., Lewin, W. H. G., Miller, J. M., & Méndez, M. 2005, *A&A*, 440, 207
- Beloborodov, A. M. 1999a, *ApJ*, 510, L123
- . 1999b, *MNRAS*, 305, 181
- Bradt, H. V., Rothschild, R. E., & Swank, J. H. 1993, *A&AS*, 97, 355
- Brocksopp, C., et al. 2006, *MNRAS*, 365, 1203
- Caballero García, M. D., et al. 2007, *ApJ*, 669, 534
- Corbel, S., Fender, R. P., Tomsick, J. A., Tzioumis, A. K., & Tingay, S. 2004, *ApJ*, 617, 1272
- Corbel, S., Fender, R. P., Tzioumis, A. K., Nowak, M., McIntyre, V., Durouchoux, P., & Sood, R. 2000, *A&A*, 359, 251
- Díaz Trigo, M., Parmar, A. N., Miller, J., Kuulkers, E., & Caballero-García, M. D. 2007, *A&A*, 462, 657
- Fender, R., et al. 1999, *ApJ*, 519, L165
- Foellmi, C., Depagne, E., Dall, T. H., & Mirabel, I. F. 2006, *A&A*, 457, 249
- Gallo, E., Fender, R. P., & Pooley, G. G. 2003, *MNRAS*, 344, 60
- Gehrels, N., et al. 2004, *ApJ*, 611, 1005
- George, I. M., & Fabian, A. C. 1991, *MNRAS*, 249, 352
- Greene, J., Bailyn, C. D., & Orosz, J. A. 2001, *ApJ*, 554, 1290
- Hjellming, R. M., & Rupen, M. P. 1995, *Nature*, 375, 464
- Homan, J., & Belloni, T. 2005, *Ap&SS*, 300, 107
- Joinet, A., et al. 2005, *ApJ*, 629, 1008
- Kuulkers, E., et al. 2000, *A&A*, 358, 993
- Magdziarz, P., & Zdziarski, A. A. 1995, *MNRAS*, 273, 837
- Malzac, J., Beloborodov, A. M., & Poutanen, J. 2001, *MNRAS*, 326, 417
- Malzac, J., et al. 2006, *A&A*, 448, 1125
- Markwardt, C. B., Smith, E., & Swank, J. H. 2005, *ATel*, 415, 1
- McClintock, J. E., & Remillard, R. A. 2006, in *Compact Stellar X-Ray Sources*, ed. W. H. G. Lewin & M. van der Klis (Cambridge: Cambridge Univ. Press), 157
- Méndez, M., Belloni, T., & van der Klis, M. 1998, *ApJ*, 499, L187
- Mitsuda, K., et al. 1984, *PASJ*, 36, 741
- Narayan, R., & Yi, I. 1995, *ApJ*, 452, 710
- Poutanen, J., & Fabian, A. C. 1999, *MNRAS*, 306, L31
- Remillard, R. A., & McClintock, J. E. 2006, *ARA&A*, 44, 49
- Rothschild, R. E., et al. 1998, *ApJ*, 496, 538
- Shakura, N. I., & Sunyaev, R. A. 1973, *A&A*, 24, 337
- Shapiro, S. L., Lightman, A. P., & Eardley, D. M. 1976, *ApJ*, 204, 187
- Shaposhnikov, N., Swank, J., Shrader, C. R., Rupen, M., Beckmann, V., Markwardt, C. B., & Smith, D. A. 2007, *ApJ*, 655, 434
- Sunyaev, R., & Titarchuk, L. 1980, *A&A*, 86, 121
- Tingay, S. J., et al. 1995, *Nature*, 374, 141
- Titarchuk, L. 1994, *ApJ*, 434, 570
- . 1997, *ApJ*, 487, 834
- Tomsick, J. A., Corbel, S., & Kaaret, P. 2001, *ApJ*, 563, 229
- Torres, M. A. P., Steeghs, D., Jonker, P., & Martini, P. 2005, *ATel*, 417, 1
- van der Hoof, F., Heemskerk, M. H. M., Alberts, F., & van Paradijs, J. 1998, *A&A*, 329, 538
- Vedrenne, G., et al. 2003, *A&A*, 411, L63
- Winkler, C., et al. 2003, *A&A*, 411, L1
- Zhang, S. H., Harmon, B. A., Paciesas, W. S., Wilson, C. A., & Fishman, G. J. 1994, *IAU Circ.*, 6106, 1
- Zhang, S. N., et al. 1997, *ApJ*, 479, 381
- Zdziarski, A. A., Poutanen, J., Paciesas, W. S., & Wen, L. 2002, *ApJ*, 578, 357
- Zdziarski, A. A., et al. 2005, *MNRAS*, 360, 825